PHYSICAL REVIEW B VOLUME 59, NUMBER 4 15 JANUARY 1999-II

In situ specular and diffuse x-ray reflectivity study of growth dynamics in quench-condensed xenon films

Ralf K. Heilmann* and Robert M. Suter
Department of Physics, Carnegie Mellon University, Pittsburgh, Pennsylvania 15213
(Received 4 June 1998)

Specular and diffuse reflectivity and diffraction of x rays are used to probe polycrystalline films of xenon quench condensed onto a SiO_2/Si substrate. Measurements during deposition complement more extensive static measurements. Stable nonequilibrium structures are observed. We interpret our observations in terms of island growth and coalescence. Island separation and ultimate size are strongly temperature dependent. Coalescence has a pronounced effect at the lowest temperature studied (17 K) where islands are small and have large surface-to-volume ratios. We observe a concurrent increase in roughness and reduction in diffuse scattering, indicating a change in surface morphology. Continued deposition yields a highly disordered, porous structure on top of the dense coalesced layer. At 25 and 35 K bulk density films grow with a surface morphology that evolves only slowly from that determined before coalescence. Bulk diffusion allows intermixing and prevents a composite film structure like that observed at lower temperatures.
[S0163-1829(99)06404-8]

I. INTRODUCTION

The process of nonequilibrium growth of solid films is of tremendous technological and scientific importance.[1] While many film/substrate systems have been characterized in great detail,[2] the basic physics of the interplay between adsorption, desorption, surface diffusion, lattice strain, crystalline anisotropy, and incident beam characteristics is not clearly understood. Its complexity is mainly due to the far-from-equilibrium growth conditions, resulting in structures that depend on many competing kinetic processes. It is this situation that motivates our study of a model system which is experimentally convenient and particularly susceptible to theoretical and computational analysis.

Films are characterized by their thickness, density, crystallinity, texture, and surface roughness, as well as by a host of properties which ultimately depend on these structural quantities. Very thin films are frequently found to consist of islands separated by a characteristic distance determined by mobility and deposition rate.[3] Islands are formed by nonwetting systems even at the lowest temperatures because deposited material always arrives with finite kinetic energy. Growth and coalescence of islands can lead to significant changes in surface morphology and roughness.[3–5] Especially surface roughness needs to be controlled in technological thin film applications due to its influence on mechanical, electronic, and magnetic properties.[1] Roughness evolution has been the focus of extensive recent work.[6,7] A dynamic scaling hypothesis, based on the apparent self-similarity of many surfaces and interfaces occurring in nature, has been proposed[8,9] and successfully applied to continuum theories of advancing interfaces, atomistic computer simulations, and a growing number of experiments.[6,7,10]

In the present study we investigate the growth kinetics of xenon films quench-condensed onto a cold, disordered substrate. All of our measurements are carried out *in situ* without the necessity of opening the deposition cell. Films are deposited, studied, and removed from the substrate whereupon a new film can be grown. Films of widely varying thickness can be deposited at different substrate temperatures and at different rates. The substrate is a silicon crystal with a regrown, 312-Å-thick, amorphous oxide layer which eliminates long-ranged epitaxial effects. The xenon atoms predominantly interact with each other and with the substrate through simple Lennard-Jones potentials.

We use x-ray reflectivity and diffraction to characterize our films. Reflectivity measures spatial variations in electron density from angstrom to micron length scales while averaging over macroscopic regions of the film. Specular reflectivity measures variations in electron density normal to the film surface, yielding information about film thickness, density, and global interface roughness. Off-specular or diffuse reflectivity is sensitive to lateral (in-plane) height correlations. Recent theoretical developments combining dynamic scaling theory and the distorted-wave Born approximation (SC-DWBA) (Refs. 11–16) to describe diffuse x-ray and neutron scattering from rough multilayers with self-affine interfaces allow, in principle, the extraction of lateral and vertical correlation lengths and roughness exponents from reflectivity data. By adding diffraction data, we are able to correlate interface properties with the crystal size and orientation distributions.

Nonequilibrium xenon films similar to ours, as well as other rare gases and their binary mixtures, have been studied by several methods. It is well established by diffraction that both thick[17,18] ($\geqslant 1$ μm) and thin[19] (10–200 Å) films are nanocrystalline and, for deposition temperatures above 5 K, have no preferred crystallite orientation. In thick xenon films,[17,18] nanocrystals have dimensions of 140 Å, lattice constants somewhat below bulk crystalline values, and the structure appears to be purely fcc. Some controversy exists as to the average mass density of these films. Reductions relative to a crystalline density of 2–4% measured by surface acoustic waves,[20] 10–13 % by ellipsometry,[21] and as much as 35% by an interferometric method[22] have been reported.

 ©1999 The American Physical Society

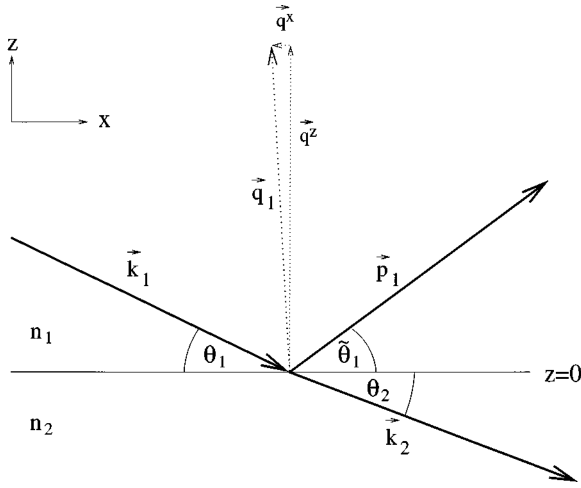

FIG. 1. Scattering geometry for reflectivity measurements (see text).

Observed large surface areas[23] make it clear that some porosity must exist. Heat capacity measurements[17,18] observe a strong enhancement relative to bulk with both tunneling and surface modes present. For xenon films, increased crystallite size has been observed in annealing experiments at temperatures near 55 K,[17–21] and films deposited at higher temperatures have properties closer to bulk values.[18]

In the next section we review the theory of x-ray reflectivity as applied in our data analysis. We then describe our experimental configuration and sample cell. Section IV presents specular and diffuse reflectivity data from films whose thicknesses span almost two orders of magnitude and that were grown at three different substrate temperatures. We correlate data taken after the deposition has ended (static data) with real-time reflectivity measurements during deposition and with diffraction line shapes from Xe Bragg peaks. We discuss the physical implications of our results in Sec. V. Conclusions are presented in Sec. VI.

II. THEORY OF X-RAY REFLECTIVITY

We give here a brief outline of the theory we have used in our data analysis. While this material appears in the literature, we present it in a consistent notation and specify the approximations we have used.

A. Specular reflectivity from stratified media

Reflection and transmission of a plane electromagnetic wave with wave vector $\vec{k_1}$ incident on a single flat interface separating two media of indices of refraction n_1 and n_2 (see Fig. 1) can be described in terms of the Fresnel theory of reflectivity[24] and can be generalized to stratified systems with multiple interfaces.[25,26] For specular reflection ($\tilde{\theta}_1 = \theta_1$) the wave vector transfer $\vec{q_1} = \vec{p_1} - \vec{k_1}$ lies along the z direction with $q_1^z = 2k_1 \sin\theta_1$. For x rays of wavelength λ we set $k_1 = p_1 = 2\pi/\lambda$, since scattering is predominantly elastic. The scattering angle 2θ is given by $2\theta = \theta_1 + \tilde{\theta}_1$. For x rays the index of refraction is written as $n \simeq 1 - \delta + i\delta'$, where $\delta = (\lambda^2 r_e \rho / 2\pi)$ and $\delta' = (\mu\lambda/4\pi)$, $r_e = 2.82 \times 10^{-5}$ Å is the classical electron radius, ρ is the effective electron number density of the medium, and $1/\mu$ is the absorption length. In general $\delta \sim 10^{-5}$ and $\delta' \sim 10^{-7} - 10^{-8}$. Total external reflection occurs whenever $\theta_1 < \theta_c \propto (\rho_2 - \rho_1)^{1/2}$.

Surface roughness is usually included in the description of x-ray reflectivity under the following assumptions: each interface can be described by a single-valued height function $h(x,y)$, and $[h(x,y) - h(x',y')]$ is a Gaussian random variable that on average only depends on the relative lateral distance $R = |\vec{R}|$, where $\vec{R} = (X,Y) = (x-x', y-y')$. The global surface roughness $\sigma(t)$ is then given by $\sigma^2(t) = \langle [h(R,t) - \langle h(t) \rangle]^2 \rangle$, where the average extends over the surface coherence area of the measurement, and t refers to deposition time or film thickness. We use the so-called "qq_t" approximation for the reflectivity,

$$R_{rough} = R_{smooth} \exp[-q_1^z q_2^z \sigma^2], \tag{1}$$

derived in the SC-DWBA,[11] as well as with a different approach by Nevot and Croce.[27] Equation (1) gives good agreement with exact dynamical calculations[26] at and below the critical angle, as long as $q_1^z \sigma \leq 1$. We have verified empirically that this approximation reproduces dynamical calculations of the specular scattering whenever layers are thicker than their bounding roughnesses and, even when this condition is violated, when bounding roughnesses are equal (the conformal limit).

B. Diffuse reflectivity in the distorted-wave Born approximation

Due to their roughness, physical interfaces scatter in nonspecular directions, with the wave vector transfer having components in the plane of the interface. The intensity distribution of diffusely scattered x rays contains information about electron density variations in the lateral direction such as interface height-height correlations. Sinha *et al.*[11] first derived an expression for the diffuse reflectivity from a single, rough, and self-affine interface in terms of its height-height correlation function $C(X,Y) \equiv \langle h(X,Y) h(0,0) \rangle$. Treatment has recently been extended to systems containing multiple interfaces.[12–16] We use the full expression for the differential cross section:

$$\left(\frac{d\sigma}{d\Omega}\right)_{diff} = \frac{L_x L_y}{16\pi^2} \sum_{j,l=1}^{N-1} (k_{j+1,c}^2 - k_{jc}^2)^* (k_{l+1,c}^2 - k_{lc}^2) \times \sum_{m,n=0}^{3} G_m^{j*} G_n^l S_{mn}^{jl}(\vec{p_\parallel} - \vec{k_\parallel}, q_{j+1,m}^z, q_{l+1,n}^z), \tag{2}$$

with the definitions $G_0^j = T_{j+1}^k T_{j+1}^p$, $G_1^j = T_{j+1}^k R_{j+1}^p$, $G_2^j = R_{j+1}^k T_{j+1}^p$, and $G_3^j = R_{j+1}^k R_{j+1}^p$. Here N is the number of layers in the model, j,l specify different interfaces, k_{jc} is the critical incident wave vector for interface j, and L_x and L_y are lateral coherence lengths with $L_x \propto 1/\sin\theta_1$ lying in the scattering plane. The T_j^k and R_j^k are unperturbed complex amplitudes of transmitted and reflected waves at the top of layer j which contain phase information describing interference effects that depend on layer thicknesses and indices of refraction.

All information about lateral correlations within and between interfaces, as well as laterally averaged interface roughnesses, is contained in the structure factors

$$S_{mn}^{jl}(\vec{q}_{\parallel},q_{j+1,m}^{z},q_{l+1,n}^{z}) = \frac{\exp\{-[(q_{j+1,m}^{z})^{*2}\sigma_j^2+(q_{l+1,n}^{z})^2\sigma_l^2]/2\}}{(q_{j+1,m}^{z})^{*}q_{l+1,n}^{z}} \times \int_{L_xL_y} dX\,dY \exp(-i\vec{q}_{\parallel}\vec{r}_{\parallel}) \times \{\exp[(q_{j+1,m}^{z})^{*}q_{l+1,n}^{z}C^{jl}(X,Y)]-1\}, \quad (3)$$

with the q_{lm}^{z} defined as $q_{l0}^{z}=p_l^z-k_l^z$, $q_{l1}^{z}=-p_l^z-k_l^z$, $q_{l2}^{z}=p_l^z+k_l^z$, and $q_{l3}^{z}=-p_l^z+k_l^z$. Here $C^{jl}(X,Y) \equiv \langle h_j(x,y)h_l(x',y')\rangle$ is the correlation function between the roughness profiles of interfaces j and l, and σ_j refers to the roughness of interface j.

In our analysis we assume interface correlations to be isotropic and use expressions appropriate for self-affine fractal surfaces.[11,28,29] Diagonal terms have the form

$$C^{jj}(R)\equiv C^{j}(R)=\sigma_j^2\exp\left[-\left(\frac{R}{\xi_j}\right)^{2\alpha_j}\right], \quad (4)$$

where α_j is the roughness exponent and interface j is characterized by a lateral correlation length ξ_j. This expression has been compared with alternative functional forms elsewhere.[30] To describe height-height correlations between different interfaces we use[28,29]

$$C^{jl}(R)=\frac{1}{2}\left(\frac{\sigma_l}{\sigma_j}C^{j}(R)+\frac{\sigma_j}{\sigma_l}C^{l}(R)\right)e^{-|z_j-z_l|/\xi_{\perp,jl}}. \quad (5)$$

Here $\xi_{\perp,jl}$ is the vertical distance over which correlations between interfaces j and l decay. $\xi_{\perp,jl}=0$ specifies uncorrelated interfaces, while $\xi_{\perp,jl}\gg|z_j-z_l|$ describes nearly perfect replication of height fluctuations. This particular form for C^{jl} includes the unphysical assumption that all spatial frequencies of the C^{j} are replicated equally between correlated interfaces.[29] However, we do not access q^x values far above 10^{-3} Å^{-1}; so our data are not expected to be sensitive to lateral length scales below 100–200 Å. For low spatial frequencies (lateral length scales much larger than film thickness) rapid changes in the degree of replication as a function of frequency seem unlikely. We therefore presume that the above simple parametrization is sufficient for a qualitative analysis of our data.

Even though the integral in Eq. (3) only becomes the Fourier transform of the correlation function in the limit of small q^z, the Fourier transform analogy between real and reciprocal space remains useful for conceptualization. Large ξ implies a small half width in q^x and vice versa. For $q^x \ll \xi^{-1}$ the diffuse intensity is constant and scales linearly with ξ. Small values of α lead to sharp cusps in the diffuse at $q^x=0$. In the limit of $q^z\sigma\ll 1$, the intensity is proportional to $\sigma^2\exp[-(q^z\sigma)^2]$: increased roughness leads to stronger diffuse scattering at small q^z.

C. Data fitting

For fitting of the specular reflectivity we employ a model consisting of a sequence of layers. Each layer is characterized by its thickness, top interface roughness, and either a chemical unit number density if the composition is known or δ and δ' otherwise. The fitting routine calculates the reflectivity in the "qq_t" approximation, convolutes the result with a finite resolution in q^z, and then minimizes the weighted mean square deviation between fit and data (χ^2). Parameters are varied by a simulated annealing algorithm using the dynamically optimized Monte Carlo (DOMC) method.[31] The fitting program has been described previously.[32,33] For our data we found that widely varying initial guesses for the fit parameters generally led to sets of parameters within the error calculated directly from the DOMC minimization. The parameters reported below have been obtained from repeated fitting runs with different starting points.

The fitting of the diffuse reflectivity is computationally demanding because the structure factors in Eq. (3) have to be integrated numerically. We use a standard nonlinear least-squares algorithm[34] in this case. For a given data set, we generally insert parameters obtained from the specular reflectivity and keep them fixed in the fitting of the diffuse data. Thus we only vary the lateral parameters α, ξ, and $\xi_{\parallel}$. Of course this approach is only expected to be successful if our model assuming Gaussian roughness and self-affine interfaces is correct. As described below, our data consist mainly of position-sensitive detector (PSD) scans (scanning 2θ at fixed θ_1) containing both diffuse and specular scattering. In most cases we simultaneously fit three PSD scans covering the accessible range of q^z and q^x, of course taking into account finite resolution in real and reciprocal space.

It has been observed[28] that the incorporation of off-specular data into fitting can lead to results that differ significantly from the best fit values obtained from analysis of the specular signal alone. Within the framework of the SC-DWBA model we find it impossible to decide for our data whether the diffuse or the specular reflectivity gives a more reliable estimate for the roughness of an interface. Discrepancies may be due to either the inappropriateness of the model for the physical system or sample inhomogeneities on length scales greater than the experimental coherence length. In such a situation the fitting will be influenced by the relative number and weighting of data points which are dominated by either the specular or the diffuse signal.

During deposition, we measure the specular reflectivity at a single, fixed angle ("real-time data"). Instead of conventional reflectivity measurements at fixed t as a function of q^z (as measured after deposition), this amounts to fixing q^z and allowing t to vary. We measure at $\theta_1=0.5°$ or $q^z=0.071$ Å^{-1}. Qualitatively, we expect to see behavior like

$$I(t)\propto e^{-[q^z\sigma(t)]^2}[1+\cos(q^z t)]+\text{const}, \quad (6)$$

with the constant depending on q^z. This expression comes trivially out of the Born approximation;[11] straightforward inclusion of phases yields expressions appropriate for layer-by-layer epitaxial growth.[35] The "growth oscillations" implied by Eq. (6) are commonly used in reflection high-energy elec-

tron diffraction[36] at large q^z where atomic scale roughness is important and have been used in other x-ray growth studies.[37]

In fitting the real-time data, we use the full ''qq_t'' approximation for the specular reflectivity with a fixed parametrization of the substrate layers. The topmost layer thickens and roughens during deposition but is assumed to have a fixed density. Based on independent measurements of the time dependence of the temperature of our Xe evaporation source we model the film growth rate vs time with an initial linear increase, followed by an exponential decay.[33] This allows us to match the locations of intensity minima and maxima in the deposition curves, which are mainly determined by film thickness and are rather insensitive to density or roughness. Given this thickness-time relation, we fit the time-dependent reflectivity amplitude to kinetic roughening models for $\sigma(t)$.

III. EXPERIMENTAL SETUP

A. Scattering configurations

Our x-ray source is a rotating anode with a copper target. The sample-cell–cryostat assembly is mounted on the Φ circle of a four-circle diffractometer. Details of the setup have been discussed elsewhere.[38] Data were taken in two different configurations. We used a bent graphite monochromator and slits to limit the beam divergence and detector acceptance in combination with a scintillation detector for medium-resolution (MR) measurements of the substrate and of Xe films up to 260 Å thick. The higher resolution necessary to resolve oscillations in the specular reflectivity for films up to 1000 Å thick was achieved with a Si(111) crystal as monochromator and slits to limit the real-space beam size and to block the Cu $K\alpha_2$ line. In this high-resolution (HR) setup we used a Braun linear PSD, which allows us to simultaneously record specular and diffuse reflectivity in the scattering plane without the need for time-consuming detector scans. The nominal position resolution of the PSD is 50 μm. The PSD counting efficiency over the 2.5 cm center section which we use is uniform to 1%. Our measured angular resolution consists of a sharp, Gaussian-like peak [0.022° half width at half maximum (HWHM)] with Lorentzian tails beginning about two decades below the central peak. The broad tails can obscure weak diffuse scattering in the neighborhood of a sharp specular peak. We restrict our analysis of diffuse scattering to cases where the diffuse-to-specular ratio is large enough that the signal is not dominated by the PSD response function.

The use of a PSD requires wide slits downstream from the sample and allows background radiation to appear at angles of $2\theta < \theta_1$. We measured this background and found it to be independent of θ_1. Its contribution is included as an incoherent background in the fitting.

B. Operation of the sample cell

The sample cell used in this study has been described previously.[33,39] As our Xe particle source we use a Grafoil sheet mounted on a thermally insulating holder inside the evacuated cell and facing the substrate at a distance of 1.5 cm (Grafoil and substrate have dimensions 5×3.8 cm^2). At temperatures below $\sim$50 K most of the loaded Xe adsorbs on the huge surface area offered by the Grafoil sheet. A heater situated behind the sheet allows us to desorb Xe, which then adsorbs on the colder substrate. Xenon atoms incident on the substrate should have an energy distribution characteristic of the Grafoil temperature (55–65 K), rather than being close to room temperature as in most prior work. The substrate is in good thermal contact with the cold finger of a closed-cycle helium refrigerator through an oxygen-free high-conductivity (OFHC) copper base, which can be heated independently. The temperature of the cell typically increases by less than 0.3 K during and subsequent to heating of the Grafoil. Our films were grown at average rates ranging from 0.1 to 10 Å/s. We see no systematic effects of the average deposition rate over this range.

IV. RESULTS

A. Substrate

We begin with reflectivity studies of the substrate onto which our Xe films are deposited. Since we re-use the same substrate for all growths, we are able to fix the structural parameters describing buried substrate layers and interfaces to those determined here. The ability to do this is a major advantage over conventional deposition systems. This is a particular advantage in x-ray reflectivity measurements where one is sensitive to buried structure.

The substrate is a Si crystal covered by a SiO_2 layer grown at high temperatures under an oxygen atmosphere. Prior to mounting, the substrate underwent a wet chemical cleaning procedure which leads to a dry surface free of contamination as shown by its homogeneous wetting behavior.[40] However, some chemisorbed water is expected to remain and some additional contamination of the high-energy surface may occur during the 30 min required to mount the substrate and seal the sample cell. Not surprisingly, the reflectivity from the ''bare'' surface (see Fig. 2) requires a two-layer model instead of just a SiO_2 layer on semi-infinite Si. The second layer has a low electron density characteristic of a patchy water film of density 0.023 H_2O/Å^3 (compared to 0.033 H_2O/Å^3 for bulk water). The SiO_2 layer has a density of 0.0215 SiO_2/Å^3, a thickness of 312.2(3) Å, and a roughness of 6.6 Å.

We developed a temperature protocol that allows us to repeatedly return to the same initial substrate condition before each film deposition.[33] The protocol is based on rapid heating of the cell and substrate to temperatures above 55 K, where Xe desorbs, followed by cooling. During this desorption cycle, the thermally isolated Grafoil remains cold enough to serve as the preferred adsorption surface in the cell. Static specular reflectivity curves out to $q^z=0.7$ Å^{-1} taken after successful desorptions are all identical within statistical errors, but are distinct from data taken with no Xe in the cell (see Fig. 2). Clearly some Xe remains on the substrate and appears to mix with the residual layer described above. We refer to the material on top of the SiO_2 as a ''base layer.'' Averaged over more than 25 films the parameters describing this layer are $\sigma=3.6\pm1.4$ Å, $t=4.1\pm3.0$ Å, and $n=3.0\pm1.5\times10^{-2}$ H_2O/Å^3.

In the presence of most Xe films the diffuse reflectivity is dominated by the vacuum/Xe interface, and the fit results

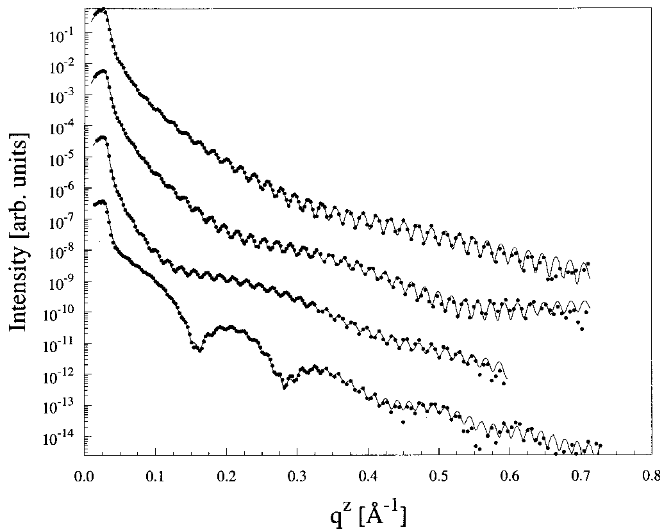

FIG. 2. Specular reflectivity from the substrate and films deposited at 17 K measured in the MR setup. Data sets are offset for clarity. Solid lines are least-squares fits yielding parameters described in the text and shown in Fig. 5. Shown are (top to bottom) reflectivities of the substrate without Xe, with a residual Xe layer (as before each deposition), and with 16- and 45-Å-thick Xe films. The rapid oscillations in the thin film data are due to the 312 Å SiO_2 layer. The superimposed oscillations are due to the deposited xenon.

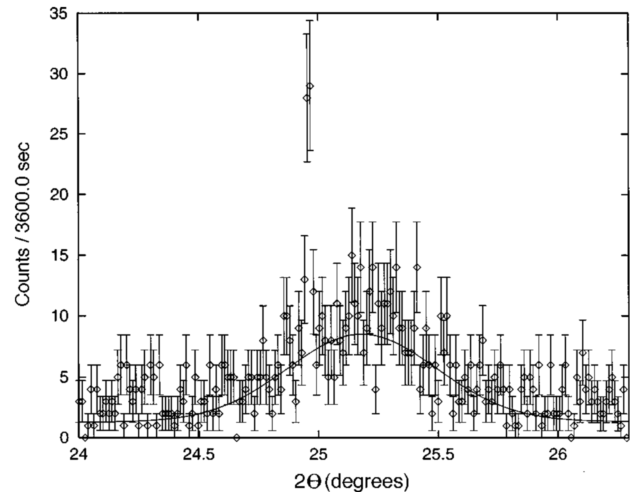

FIG. 3. The Xe(111) diffraction peak from a 1100- (100-) Å-thick film. The peak position yields an fcc lattice constant of 6.11 Å. Data were collected in 1 h using the PSD. The solid line is a fit to a Gaussian plus linear background. The two high data points are from the substrate Si(111) crystal truncation rod and indicate the resolution of the measurement.

differ negligibly when the SiO_2 and base layer parameters vary over a broad range. In the analysis below, we use $\alpha = 0.27$ and $\xi = 550$ Å for the top SiO_2 interface, as obtained from fits of the diffuse reflectivity in the absence of Xe in the cell. Diffuse scattering from the SiO_2/Si interface can be neglected due to its small roughness and electron density contrast. Measurable contributions from the Xe/base layer interface were found to be sensitive to the base layer density, but not to the lateral parameters (we used $\alpha = 0.25$–0.5, $\xi = 100$–200 Å), and appeared only at larger q^x, where our counting statistics are low.

The initial nucleation process on any substrate depends on many microscopic features. Even with a ''bare'' amorphous oxide surface, it would be difficult to estimate, for example, the density of pinning sites or the preferred location for nuclei. Our ''base layer'' is a complication for data analysis, but it does not necessarily change the film growth phenomenology. We are depositing onto a random but statistically repeatable substrate structure.

It may be interesting to note that on some occasions before our temperature protocol was fully developed, we would observe very strong diffuse scattering and strong and narrow Xe Bragg peaks. Clearly, at elevated temperatures, we could grow large Xe crystals. However, on some of these occasions, the specular signal was essentially indistinguishable from that of a well-prepared surface with small roughness. We attribute this situation to an inhomogeneous surface with acceptably clean regions coexisting with a distribution of Xe crystals. The specular signal is dominated by the flat regions while the diffuse scattering comes from the roughness due to crystals. Thus, diffuse scattering is a sensitive probe of surface heterogeneity. It is this scattering that we monitor to assure that the substrate is ready for film deposition.

B. Xenon films

Diffraction data indicate that, over the entire temperature range studied, the films are polycrystalline, three-dimensional powders. Figure 3 shows a diffraction peak from a 17 K deposition. The signal even from this 1100-Å-thick film is quite weak and broad. The width corresponds to a finite size[41] of $\pi/\delta q = \pi/(2k \cos\theta\delta\theta) = 150(15)$ Å, where δq and $\delta\theta$ are half widths at half maximum. Widths are independent of film thickness for $t \geqslant 400$ Å but appear broader for thinner films (where, however, our counting statistics are poor). Similar data using a variety of incident angles indicate no texture or preferred crystallite orientation. Average crystallite sizes of 140 Å have previously been observed via x-ray diffraction on micron thick Xe films quench-condensed onto quartz at temperatures as low as 6 K.[17,18] Thus the crystallinity of the films does not depend on thickness, on details of substrate structure, or on temperature over the range from 6 to 35 K.

Our most extensive data were collected on xenon films deposited at the base temperature of our cryostat which varied from 16 to 18 K. Since no temperature dependence over this range was discerned, we refer to these together as 17 K depositions. Films held at the base temperature were stable over periods of days as verified by repeated specular reflectivity measurements.[33] Although heat capacity measurements indicate some kinetics in similarly prepared films at even lower temperatures,[17,18,20] these are presumably local relaxations which do not affect our measurements.[42]

Figures 2 and 4 show specular reflectivity data from several films deposited at 17 K. The varying oscillation frequency superimposed on the substrate signal corresponds to varying xenon film thickness. As the oscillation frequency increases, the reflectivity signal decays more rapidly with q^z, indicating increasing roughness. The useful range in scattering angle for the analysis of thick, rough films does not extend to large q^z due to this loss of signal.

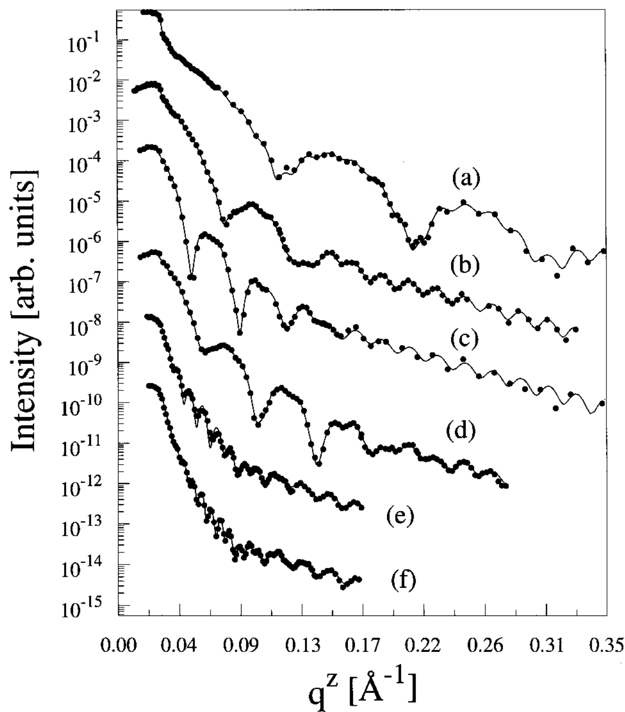

FIG. 4. Specular reflectivity measured in the HR setup. From the fits we obtain total Xe film thicknesses of (a) 63 Å, (b) 104 Å, (c) 166 Å, (d) 140 Å, (e) 565 Å, and (f) 826 Å. All films except (d) were measured after deposition at 17 K. (d) is the same film as (c) but after 10 h of annealing at 25 K.

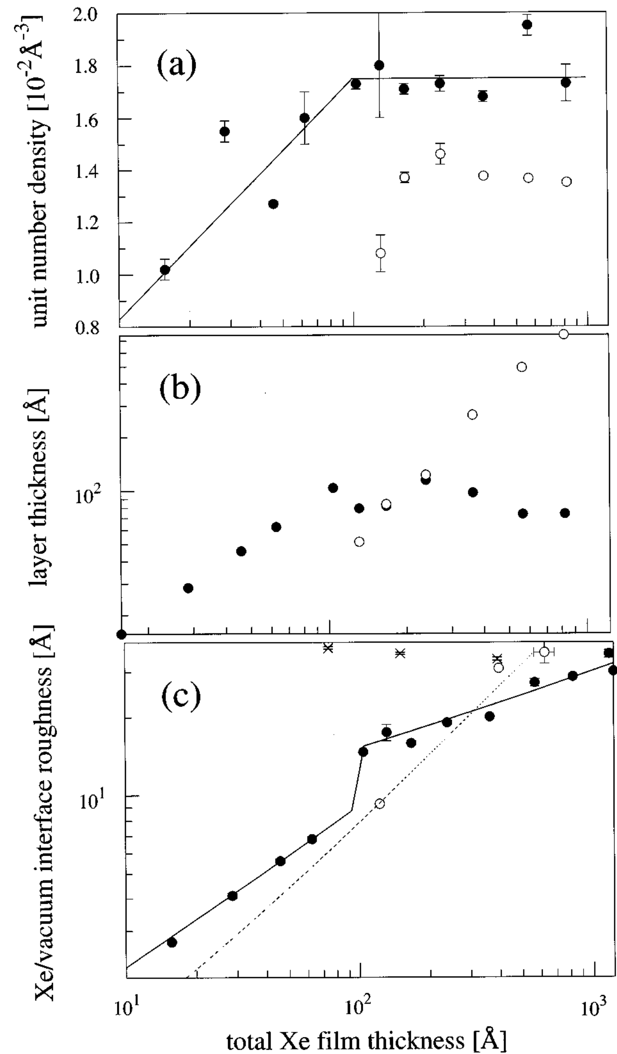

FIG. 5. Fitting parameters vs total thickness for films deposited at 17 K. (a) shows xenon layer densities for the layer next to the substrate (solid circles) and for the upper layer when a two-layer model was used (open circles). (b) shows xenon layer thicknesses using the same conventions as (a). (c) shows the xenon/vacuum interface roughness (solid circles). The solid line consists of three parts. The left and right sections are power law fits to the data with exponents of 0.66 and 0.33. The middle section was chosen as a connection of the fast and slow roughening regimes that also fits the real-time deposition data shown in Fig. 8. The open circles are for films grown at 25 K. The dash-dotted line has an exponent of 0.9 which was deduced from fits to real-time deposition data (see Fig. 10). The crosses are results from films grown at 35 K.

The quantitative least-squares fits illustrated in Figs. 2 and 4 yield a detailed picture of the film growth process. For the total of five xenon films with thickness t less than ≈ 100 Å, a single uniform xenon layer on top of the substrate (modeled as described above) suffices to yield fits with reduced $\chi^2 < 3$ in all but one case. For thicker films, additional structure is required. We introduce a second xenon layer and allow the thickness, roughness, and density of both layers to vary in the fits. Figure 5 shows the evolution of fitting parameters with total xenon film thickness.

Figure 5(a) shows evidence for increasing Xe number density as t increases in the region $t < 100$ Å. Using the diffraction data of Fig. 3, a lattice constant of 6.11(6) Å or a number density of $n = 0.0175(2)$ Xe/Å^3 is inferred for xenon crystals at this temperature. Thus, near $t = 100$ Å films approach crystalline or bulk density. As shown in Figs. 5(a) and 5(b), for $t > 100$ Å, fits indicate a dense bottom layer with essentially crystalline density and 100 Å thickness under the growing top layer. The interface width between the xenon layers is 20(2) Å (over six measured films) and exhibits no trend with thickness.

The evolution of the surface roughness σ with xenon film thickness is shown in Fig. 5(c). Rapid roughening, which can be parametrized by $\beta = 0.66(1)$, takes place at low coverage. Near $t = 100$ Å, just where the film structure becomes complex, an almost discontinuous increase in σ by about a factor of 2 appears. Thicker films roughen more slowly, with $\beta = 0.33(2)$. The discontinuity in σ is also seen in fits using only a single Xe layer; it is not an artifact of changing models. Also, the films were grown in essentially a random sequence; the discontinuity is not due to a change in the character of the substrate or apparatus.

Diffuse scattering from films deposited at 17 K also distinguishes thin films from thicker ones. Figures 6 and 7 show PSD scans from 28 and 565 Å films, respectively. Measurable diffuse intensity extends beyond $\theta_1 = 2°$ for the thin film but only to 1° for the thicker one. We are not able to obtain good fits to the thin film data, whereas for $t > 100$ Å, the power law model (Sec. II) gives acceptable agreement. For $t > 100$ Å, the diffuse scattering is nearly independent of t and the intensity is constant at constant q^z out to our maximum q^x values; this implies $\xi < 500$ Å. Power law fits using $\xi \approx 100$ Å yield $0.1 < \alpha < 0.5$. This

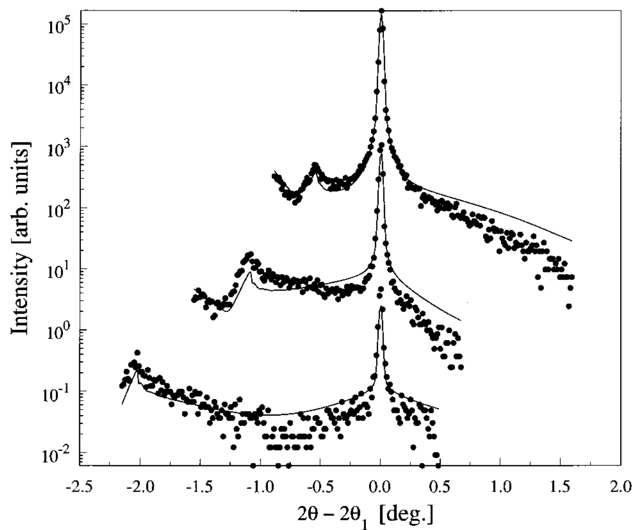

FIG. 6. PSD scans from a $t=28$ Å film deposited at 17 K. $\theta_1=0.750°$, $1.300°$, and $2.238°$ (top to bottom). To obtain reflectivity the data need to be divided by 4.68×10^8, 4.68×10^7, and 4.68×10^6 (top to bottom). For comparison, the solid line uses the SC-DWBA with $\alpha=0.3$ and $\xi=516$ Å for the Xe/vacuum interface, and $\xi_\perp=100$ Å to describe correlations with the Xe/SiO_2 interface.

variation in α is required to keep the diffuse intensity the same as the roughness (as measured by specular data) increases.

Real-time specular measurements at $\theta_1=0.5°$ (see Fig. 8) further corroborate the evolution of roughness presented above but also imply that slow kinetics may be relevant at $T=17$ K. The data points (open circles) taken from static post-deposition measurements agree with the real-time data for $60<t<300$ Å (50–150 s). The single-layer fit, using the roughness vs thickness curve obtained from static measurements, reproduces the real-time and static data in this

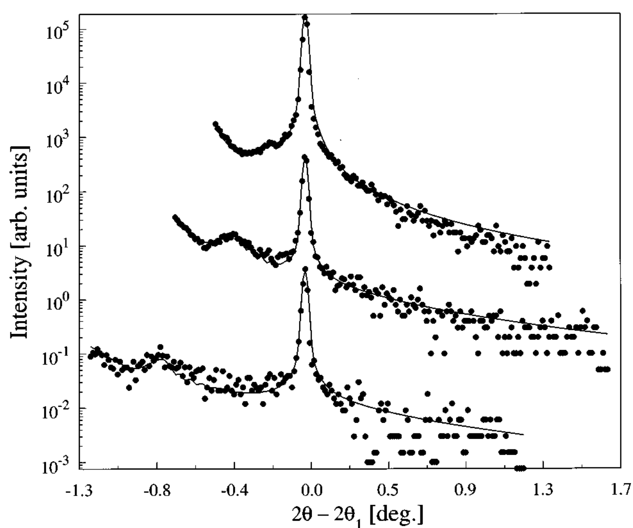

FIG. 7. PSD scans from a $t=565$ Å film deposited at 17 K. $\theta_1=0.418°$, $0.606°$, and $0.994°$ (top to bottom). To obtain reflectivity the data need to be divided by 1.35×10^8, 1.35×10^7, and 4.05×10^5 (top to bottom). Apart from conformality oscillations (which decay with $\xi_\perp\sim150$ Å) this diffuse scattering is characteristic, in magnitude and form, of all films with $t>100$ Å.

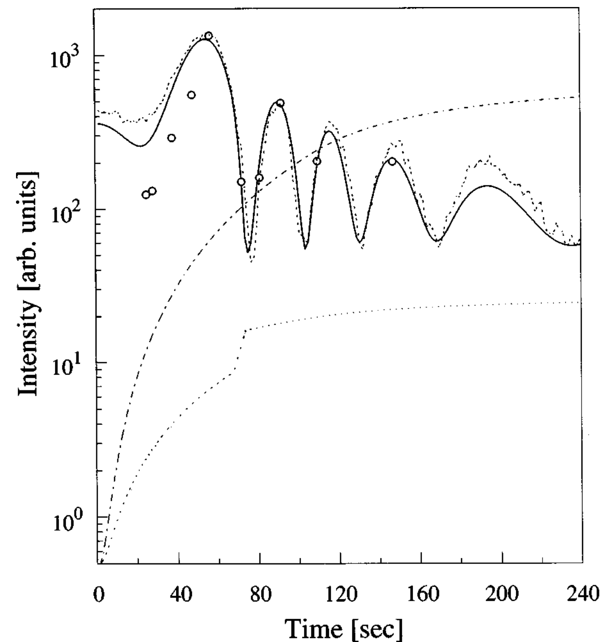

FIG. 8. Reflectivity at $q^z=0.071$ Å^{-1} ($\theta_1=0.5°$) as a function of time during deposition at 17 K (short-dashed line). The reflected intensity was measured for one second every 1.5 s. This curve is highly repeatable for depositions at this temperature (Refs. 33 and 39). The solid line is a fit using a single xenon density of 0.0170 Xe/Å^3 and roughness (dotted line) and thickness (dash-dotted line) in angstrom as a function of time as shown. The relation between roughness and thickness is taken from Fig. 5(c). The sudden increase in roughness close to $t=100$ Å is necessary to model the steep drop in reflectivity at the first minimum. The open circles show the reflectivity at this q^z taken from static measurements of complete films of the corresponding thicknesses. Thus, the open circles represent long-time behavior in contrast to real-time behavior.

region. The disagreement between real-time and static data at early times indicates an evolution in film structure over times scales of at least seconds. Most likely, this is due to roughening as the islands grow.

Deposition at 25 K yields behavior similar to that observed at 17 K. Three films, ranging in thickness from 122 Å to ≈600 Å, were studied. To minimize potential annealing effects the cell was cooled to 17 K immediately after deposition and before static measurements. Specular reflectivities at these thicknesses (Fig. 9) can be fit using a single xenon layer of bulk density [0.0174(5) Xe/Å^3 for the three measurements], although some improvement is obtained for the thickest film if we use a two-layer model. Deduced roughnesses are shown in Fig. 5(c). Diffuse scattering (not shown) from the thinnest film (here over 100 Å thick) is the strongest of the three and cannot be fit satisfactorily by the power law model. The two thicker films with weaker diffuse scattering can be fit reasonably well and yield unresolved small values of ξ. Real-time data for deposition (Fig. 10) up to 400 Å are consistent with uniform film density and a steep power law, $\beta=0.9(1)$. It can be seen in Fig. 5(c) that this result is consistent with the roughness evolution derived from static measurements. Thus at 25 K kinetic time scales are less than or on the order of seconds: real-time and static measurements see the same film structure. Our data do

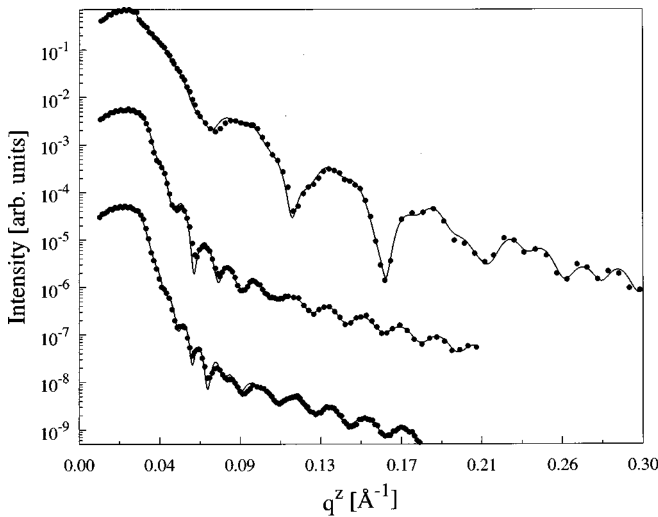

FIG. 9. Specular reflectivity from films deposited at 25 K, shifted for clarity. From the top down, the films are 122, 397, and 624 Å thick.

not rule out the possibility of a jump in roughness before $t = 400$ Å which may accompany the decrease in diffuse scattering just as it does in lower temperature depositions.

Depositions at $T = 35$ K exhibit rapid roughening followed by saturation and strong diffuse scattering. Figure 5(c) shows the roughnesses obtained from three static measurements (again carried out at 17 K, not shown). No indication of internal structure is evident.[33] Figure 10 shows entirely consistent behavior in measurements during deposition. The initial drop in reflectivity indicates rapid roughening while the essentially constant envelope at later times indicates constant roughness as the film thickens. Among all films, those grown at 35 K show the strongest diffuse scattering. We do not obtain good fits to the diffuse scattering at any thickness, with the worst deviations being at smaller thickness.

To better understand the strongly nonequilibrium behavior discussed above, we carried out annealing studies of two

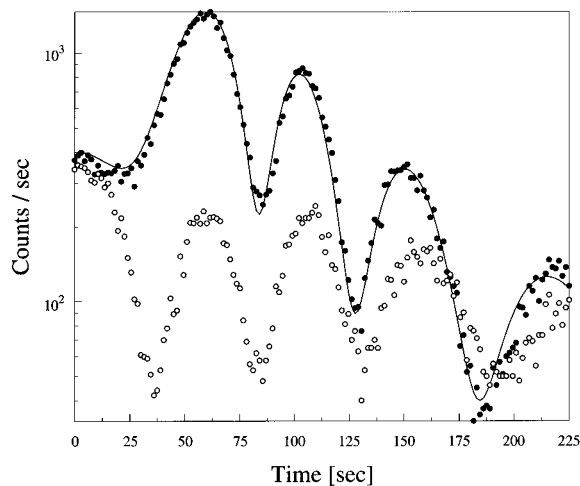

FIG. 10. Real-time reflectivity measured at $q = 0.071$ Å^{-1} during xenon deposition onto a substrate held at 25 K (solid circles) and 35 K (open circles). The final thickness of both films is about 400 Å. The solid line through the 25 K data is a fit which is discussed in the text.

of the films deposited at 17 K. These films were initially 166 Å (case 1) and 346 Å (case 2) thick and were annealed at 25 K for 10 h. By monitoring the reflectivity at $q^z = 0.071$ Å^{-1} during the annealing, we found that rapid changes take place during the first 30–60 min, but that the structure continues to evolve during the entire annealing period. From static reflectivity measurements after annealing [case 1; see Fig. 4(d)], we make the following observations: (1) Material is conserved, indicating negligible desorption at 25 K. The amount of xenon per unit area is given roughly by $\Sigma t_i n_i$, where t_i and n_i are the thickness and number density of layer i. For case 1, we obtain 2.55 Å^{-2} before the anneal and 2.53 Å^{-2} after. Case 2 had 5.29 Å^{-2} before and 5.26 Å^{-2} after. (2) Both initial films, being thicker than 100 Å, required two-layer models to fit the reflectivity. Upon annealing, the denser bottom layer became thicker at the expense of the top layer. For case 1, only one layer of bulk density was required to fit the annealed film data. This single layer is 16% thinner than the unannealed film. The roughness of the external surface was reduced from 16 to 12 Å. In case 2, annealing was incomplete in that two Xe layers remained. The bottom layer thickened from 97 to 122 Å; the top layer thinned from 266 to 225 Å. Both layers maintained their initial densities and interface roughnesses to within errors (although even the two-layer fit to the annealed film contains systematic deviations from the data). (3) In case 1, the intensity of the diffuse reflectivity is markedly increased after annealing despite the smaller roughness. This change can be only partially explained by the different density contrast at the Xe surface; i.e., the lateral correlations must have changed as well. Both before and after annealing we obtain reasonable fits with $\xi \approx 60$–90 Å for the Xe surface and $\xi_\perp \approx 200$–300 Å. However, we find $\alpha = 0.18$ before and $\alpha = 0.11$ after annealing. In case 2 very little change is observed in the diffuse scattering.

V. DISCUSSION

The data presented above point to a global picture of nonequilibrium Xe film growth at low temperatures: solid Xe does not wet the substrate and therefore at low coverage forms islands which give rise to strong diffuse scattering. The characteristic size and separation of islands depend strongly on the substrate temperature. At sufficiently high coverage, the islands coalesce into a continuous film. At low T, coalescence causes an abrupt change in surface morphology and roughening kinetics. The point at which this crossover is observed should depend on temperature primarily through the island morphology and average separation distance. The growth of our Xe films is in many ways similar to the growth of other nonwetting systems.[1–5]

At 17 K, several observations point to island growth, coalescence, and post-coalescence growth. Two distinct growth regions occur: for thin films ($t < 100$ Å), roughness increases rapidly, diffuse scattering is strong and non-power-law like, and the laterally averaged film density increases toward that of bulk xenon. This is the island growth regime. Quantitative interpretation of the roughening is made complicated by the underlying substrate roughness and the possibility of intermixing of xenon with the residual layer on the substrate surface. What is clear is that the xenon must be

forming three-dimensional islands with a characteristic separation of ~ 100 Å. When the laterally averaged thickness approaches 100 Å, a dramatic restructuring of the film occurs. Film density reaches that of bulk xenon, the roughness increases by a factor of 2 but diffuse scattering is reduced and becomes consistent with a power law model, and thicker films have a composite structure. Coalescence has occurred, and with it a release of binding energy, allowing the film to achieve a relatively ordered structure. The increase in roughness may indicate a degree of microfaceting. This rough layer serves as an inert substrate for the deposition of additional material. The top layer grows to hundreds of angstroms with a density reduced from that of bulk Xe by $\approx 18\%$. Roughening proceeds more slowly, with $\beta \approx 1/3$, indicating more uniform distribution of deposited material. The observed value of β is somewhat larger than numerical results for the equation of Kardar, Parisi, and Zhang,[6] but falls within the range obtained in other growth experiments on continuous films.[6,7]

The observation that the film has a dense layer at the substrate may explain the conflict between previous mass density measurements. Since surface acoustic waves[20] are dominated by the near-surface region of the film, our observation of a bulk-density 100 Å-thick layer appears consistent with the small deviation from bulk density given in Ref. 20. Our observed density for the upper film lies between the results of Loistl and Baumann[21] and Schulze and Kolb.[22] The remaining differences may reflect the different substrates being used in these studies.

At higher deposition temperatures, we expect increased surface diffusion to lead to larger, more widely separated islands. At 25 K, we see a steep power law $\beta \sim 0.9$, implying rather columnar growth. Based primarily on real-time data, it appears that rapid growth extends to larger thickness and roughness than at 17 K. For thinner films, we see the strong diffuse scattering expected from islands. This diffuse scattering remains flat over the limited q^x range accessed. In the thickest film studied, the diffuse intensity is reduced in magnitude, implying a change in morphology analogous to that observed at low T. On the other hand, both real time and static reflectivity are consistent with the nearly bulk density over this same thickness range. Static data on thinner films, where the coverage is expected to be more sparse, may clarify this situation. No composite layer structure is observed at elevated temperatures as is consistent with the mobility implied by the observed annealing behavior and with that reported in the literature.[17,18,20]

The presence of larger islands, atomic mobility, and bulk film density is consistent with specific heat measurements on films deposited or annealed near this temperature.[17,18] These data show a reduced T^2 contribution compared to lower-temperature films. This is interpreted as reduced porosity and surface area as required by our data.

At 35 K deposition yields large roughness for quite thin films. At this temperature, the surface diffusion length is large; we expect widely separated islands which grow large as deposition proceeds. In a simple model of three-dimensional island growth, $\sigma/t \sim (L/t)^{1/3}$ for well-separated islands,[43] with L being the island separation or the surface diffusion length. Since L increases rapidly with temperature, larger σ/t is expected at higher temperatures. While our data extend across the regime where the density saturates at the bulk value, we see no significant restructuring of the surface. This can be understood from the expected large island size: a small surface-to-volume ratio reduces the energy released per atom when islands come into contact and makes coalescence ineffective in changing the film structure. Qualitative analysis of diffuse scattering indicates structure consistent with a large surface correlation length corresponding to large islands. Deposition after coalescence yields only subtle changes in surface roughness.

Annealing at 25 K of films deposited at low temperature indicates that slow bulk diffusion occurs at this temperature. This is evident from the advance of the dense-to-disordered interface toward the film surface. During 25 and 35 K depositions, this mobility allows a dense layer to grow on the coalesced film and no complex internal film structure forms.

It is noteworthy that a characteristic ''crystallite coherence length'' of ≈ 150 Å seems to exist for xenon films grown at temperatures from 5 K (Refs. 17 and 18) up to 35 K. Given the broad temperature range and atomic mobility at the upper end of this range, it appears likely that crystal defects such as stacking faults may limit the diffraction peak widths.[41] Annealing of stacking faults requires the coordinated motion of many atoms and involves small gains in binding energy. This mechanism would decouple Bragg peak widths from the island or cluster sizes. By 50 K, this length for Xe has increased by at least a factor of 3 judging from Fig. 1 of Steinmetz *et al.*[18] Low-temperature coherence lengths exist for other rare gases as well:[17] 160 Å for Kr and 330 Å for Ar.

VI. CONCLUSIONS

We have demonstrated that stable, nonequilibrium noble gas films can be grown in a relatively simple x-ray sample cell. On our disordered substrate the growth is analogous to more conventional and technologically important deposition systems. In contrast to these latter systems, the ease and repeatability of noble gas film preparation allows the study of many films deposited under nearly identical or systematically varied conditions without heroic sample preparation efforts. The variety of scattering techniques used here (specular reflectivity, off-specular diffuse scattering, static and real-time measurements, and Bragg diffraction) yields an extensive characterization of growth kinetics. We look forward to extending these measurements to a more detailed mapping of the observed temperature dependent growth behavior as well as to other systems.

We undertook to study as simple a nonepitaxial deposition system as possible. The results indicate that even such a simple system exhibits substantial complexity. Three distinct although connected behaviors are observed at the three temperatures probed and structural variations are observed as a function of film thickness. Thus, physical effects (in contrast to chemical bonding) are sufficient to generate complex behavior under these far-from-equilibrium conditions; this is certainly not surprising given the large body of theoretical and experimental literature on deposition problems.[6,7] However, coarse-grained dynamic scaling theories certainly do not describe most of the behavior observed here. We find that the power law model based on dynamic scaling yields reasonable fits to data from individual continuous films, but

the exponents obtained are not independent of film thickness or temperature.

The present work can be extended in a number of ways. The use of synchrotron radiation sources would make feasible a variety of rapid data collection techniques. For example, energy dispersive scattering[44] will allow real-time measurements covering a large section of the specular reflectivity rather than the single value of q^z used in Figs. 8 and 10. Measurement of diffuse scattering out of the specular plane[45] allows collection of data at large q^x which should make it possible to track small islands sizes. Furthermore, the physics of a variety of other classes of deposition system can be studied. Atomically flat and ordered substrates can be used as can substrates which are wetted by the deposited material. Volatile molecular species can be substituted for the noble gas. Clearly, the combination of x-ray techniques with scanning probe microscopies would be invaluable. In addition, computer simulations with relevant interaction potentials would yield complimentary information about atomic mobilities, island conformations, and coalescence phenomena.

ACKNOWLEDGMENTS

We are grateful for helpful discussions with M. A. Knewtson, F. Family, S. Garoff, and B. Keister. Our thanks go to J.-P. Schlomka and O. H. Seeck for making the data and fits from Ref. 28 available to us for the testing of our diffuse reflectivity fitting program.

*Present address: Division of Engineering and Applied Sciences, Gordon McKay Laboratory, Harvard University, Cambridge, MA 02138.

[1] See for example, *Evolution of Surface and Thin Film Microstructure*, edited by H. A. Atwater *et al.*, MRS Symposia Proceedings No. 280 (Materials Research Society, Pittsburgh, 1992); *Disordered Materials and Interfaces*, edited by H. E. Stanley, H. Z. Cummins, D. J. Durian, and D. L. Johnson, MRS Symposia Proceedings No. 409 (Materials Research Society, Pittsburgh, 1996).

[2] Some recent examples are (a) H. Zeng and G. Vidali, Phys. Rev. Lett. **74**, 582 (1995); (b) H. You, R. P. Chiarello, H. K. Kim, and K. G. Vandervoort, *ibid.* **70**, 2900 (1993); (c) J. A. Stroscio, D. T. Pierce, and R. A. Dragoset, *ibid.* **70**, 3615 (1993); (d) R. Chiarello, V. Panella, J. Krim, and C. Thompson, *ibid.* **67**, 3408 (1991).

[3] K. L. Chopra, *Thin Film Phenomena* (McGraw-Hill, New York, 1969).

[4] B. Müller, L. Nedelmann, B. Fischer, H. Brune, J. V. Barth, and K. Kern, Phys. Rev. Lett. **80**, 2642 (1998).

[5] F. M. Ross, J. Tersoff, and R. M. Tromp, Phys. Rev. Lett. **80**, 984 (1998).

[6] A.-L. Barabási and H. E. Stanley, *Fractal Concepts in Surface Growth*, 1st ed. (Cambridge University Press, England, Cambridge, 1995), and references therein.

[7] J. Krim and G. Palasantzas, Int. J. Mod. Phys. B **9**, 599 (1995).

[8] F. Family and T. Vicsek, J. Phys. A **18**, L75 (1985).

[9] F. Family, Physica A **168**, 561 (1990).

[10] *Dynamics of Fractal Surfaces*, 1st ed., edited by F. Family and T. Vicsek (World Scientific, Singapore, 1991).

[11] S. K. Sinha, E. B. Sirota, S. Garoff, and H. B. Stanley, Phys. Rev. B **38**, 2297 (1988).

[12] V. Holý, J. Kuběna, I. Ohlídal, K. Lischka, and W. Plotz, Phys. Rev. B **47**, 15 896 (1993).

[13] V. Holý and T. Baumbach, Phys. Rev. B **49**, 10 668 (1994).

[14] S. K. Sinha, J. Phys. III **4**, 1543 (1994).

[15] S. Dietrich and A. Haase, Phys. Rep. **260**, 1 (1995).

[16] D. K. G. deBoer, Phys. Rev. B **53**, 6048 (1996).

[17] H. Menges and H. v. Löhneysen, J. Low Temp. Phys. **84**, 237 (1991).

[18] N. Steinmetz, H. Menges, J. Dutzi, H. v. Löhneysen, and W. Goldacker, Phys. Rev. B **39**, 2838 (1989).

[19] S. I. Kovalenko, E. I. Indan, and A. A. Khudoteplaya, Phys. Status Solidi A **18**, 235 (1972).

[20] L. Hornig, B. Döttling, G. Weiss, S. Hunklinger, and F. Baumann, Z. Phys. B **86**, 217 (1992).

[21] M. Loistl and F. Baumann, Z. Phys. B **82**, 199 (1991).

[22] W. Schulze and D. M. Kolb, J. Chem. Soc., Faraday Trans. 2 **70**, 1098 (1974).

[23] V. B. Yuferov and P. M. Kobzev, Sov. Phys. Tech. Phys. **14**, 1261 (1970).

[24] J. D. Jackson, *Classical Electrodynamics*, 2nd ed. (John Wiley & Sons, New York, 1975).

[25] M. Born and E. Wolf, *Principles of Optics*, 1st ed. (Pergamon Press, New York, 1959).

[26] L. G. Parrat, Phys. Rev. **95**, 359 (1954).

[27] L. Nevot and P. Croce, Rev. Phys. Appl. **15**, 761 (1980).

[28] J.-P. Schlomka, M. Tolan, L. Schwalowsky, O. H. Seeck, J. Stettner, and W. Press, Phys. Rev. B **51**, 2311 (1995).

[29] J. Stettner, L. Schwalowsky, O. H. Seeck, M. Tolan, W. Press, C. Schwarz, and H. v. Känel, Phys. Rev. B **53**, 1398 (1996).

[30] G. Palasantzas and J. Krim, Phys. Rev. B **48**, 2873 (1993).

[31] D. Bouzida, S. Kumar, and R. H. Swendsen, Phys. Rev. A **45**, 8894 (1992).

[32] W. R. Birch, M. A. Knewtson, S. Garoff, R. M. Suter, and S. Satija, Colloids Surf., A **89**, 145 (1994); Langmuir **11**, 48 (1995).

[33] R. K. Heilmann, Ph.D. thesis, Carnegie Mellon University, 1996.

[34] P. R. Bevington, *Data Reduction and Error Analysis for the Physical Sciences* (McGraw-Hill, New York, 1969).

[35] See, for example, D. M. Kelly, E. E. Fullerton, J. Santa-Maria, and I. K. Schuller, Scr. Metall. Mater. **33**, 1603 (1995).

[36] J. H. Neave, B. A. Joyce, P. J. Dobson, and N. Norton, Appl. Phys. A: Solids Surf. **31**, 1 (1983).

[37] P. Dai, T. Angot, S. N. Ehrlich, S. K. Wang, and H. Taub, Phys. Rev. Lett. **72**, 685 (1994); R. L. Headrick, S. Kycia, Y. K. Park, A. R. Woll, and J. D. Brock, Phys. Rev. B **54**, 14 686 (1996).

[38] J. D. Shindler and R. M. Suter, Rev. Sci. Instrum. **63**, 5343 (1992).

[39] R. K. Heilmann and R. M. Suter, in *Disordered Materials and Interfaces* (Ref. 1), p. 239.

[40] B. Frank and S. Garoff, Langmuir **12**, 675 (1996).

[41] B. E. Warren, *X-ray Diffraction* (Dover, New York, 1990).

[42] The minimum length scale probed in the direction normal to the film plane, L^z_{min}, corresponds to $2\pi/q^z_{max}$. Typically $q^z_{max} \leqslant 0.7$ Å^{-1} and $L^z_{min} \geqslant 9$ Å. However, scattering measurements are sensitive only to modulations in the *laterally averaged* electron density (the electron density averaged over the coherence area perpendicular to the scattering vector $\vec{q}$). The extent of this

lateral averaging is determined by the resolution. In the reflectivity regime, the averaging length extends to micron scales within the scattering plane (L^x) but only a few Angstroms in the out-of-scattering-plane direction (L^y). Due to the one-dimensional averaging in L^x, we do not expect to be sensitive to local, tunneling-level relaxation.

[43] For three-dimensional objects, the average thickness scales as the linear dimension times the fraction of surface area covered: $\langle t \rangle \sim R(R/L)^2$ where R is the linear dimension of an island and L is the average island spacing. Thus, $R \sim L^{2/3} t^{1/3}$. The mean-squared height scales as $\langle t^2 \rangle \sim R^2(R/L)^2$. The mean-squared roughness therefore goes like $\sigma^2 \sim (R^4/L^2)[1-(R/L)^2]$ and $\sigma \sim L^{1/3} t^{2/3}$ for $R/L \ll 1$. Thus, $\sigma \sim t^{2/3}$ as long as L is fixed, i.e., for a fixed number of islands.

[44] D. H. Bilderback and J. Hubbard, Nucl. Instrum. Methods Phys. Res. **195**, 85 (1982); **195**, 91 (1982); E. Chason and D. T. Warwick, in *Advances in Surface and Thin Film Deposition*, edited by T. C. Huang, P. I. Cohen, and D. J. Eaglesham, MRS Symposia Proceedings No. 208 (Materials Research Society, Pittsburgh, 1991), p. 351; B. K. Tanner, S. J. Miles, D. K. Bowen, L. Hart, and N. Loxley, *ibid.*, p. 345.

[45] T. Salditt, T. H. Metzger, and J. Peisl, Phys. Rev. Lett. **73**, 2228 (1994).